



Effect of Surface pH on Electrodeposited Ni Films

M. Motoyama,^a Y. Fukunaka,^{a,*} T. Sakka,^{b,*} and Y. H. Ogata^{b,*}

^aDepartment of Energy Science and Technology, Kyoto University, Yoshida-honmachi, Sakyo, Kyoto 606-8501, Japan

^bInstitute of Advanced Energy, Kyoto University, Uji, Kyoto 611-0011, Japan

Ni metal was potentiostatically electrodeposited on a vertical plane cathode in a Watts bath in order to determine the effect of the cathode surface pH on the Ni film microstructure. Polarization curves and current efficiencies were measured at pH values of 1.5, 3.4, and 5.5. The surface pH value (pH^s) was estimated from the measured partial current density for hydrogen gas evolution based on a steady-state one-dimensional mass transfer model. Any species relating to the buffering function through the dissociation reactions (HSO_4^- , H_3BO_3 , $\text{Ni}_4(\text{OH})_4^{4+}$, H_3O^+ , OH^-) were taken into account. The pH^s abruptly rose to above 6 as the partial current density for H_2 gas evolution increased. The preferred orientation of electrodeposited Ni thin film was plotted in electrode potential- pH^s diagram. It was found that the transition boundary between {110} and {100} preferred orientations was located along a ridge 500 mV below the H^+/H_2 equilibrium potential line. This relationship suggests that the dissolved hydrogen atoms in Ni metal are partly responsible for the evolution of structural texture of the Ni films.

© 2006 The Electrochemical Society. [DOI: 10.1149/1.2196672] All rights reserved.

Manuscript submitted December 19, 2005; revised manuscript received February 27, 2006. Available electronically May 17, 2006.

Electrodeposited Ni metal films are used for protective coatings on carbon steels. Such films also have been applied to microelectromechanical systems (MEMS)^{1,2} as well as magnetic recording heads^{3,4} and ultrathin films for magnetic sensors.⁵ The textured structure of electrodeposited Ni metal films is known to evolve as a result of nucleation and growth processes, depending on the electrolytic conditions, e.g., the electrolyte composition, pH, bath temperature, current density, stirring condition, and organic additives. The specific structure determines the physicochemical and mechanical properties of Ni films. Much more effort to improve the microcrystalline structure of high-area electrodeposited films is also necessary in the field of advanced energy science. Doing so leads to a highly functionalized catalytic electrode by tailoring a unique interface that is required for efficient energy conversion.

In spite of many works,⁶⁻¹⁷ the mechanism of Ni electrodeposition has not been thoroughly understood. Because the Ni^{2+}/Ni system has a more negative equilibrium potential ($E^0 = -0.23$ V) than the H^+/H_2 couple, H_2 gas evolution inevitably accompanies Ni metal electrodeposition. The pH value in the neighborhood of the cathode increases as the H^+ ions are reduced to evolved H_2 gas.

The Centre National de la Recherche Scientifique (CNRS) research group investigated the correlations between the microstructure of Ni films electrodeposited from a Watts bath and the electrolytic conditions.⁶⁻¹⁰ They considered the inhibiting influences of hydrogen adatoms (H_{ads}), H_2 molecules, and the stabilization of $\text{Ni}(\text{OH})_2$ on the cathode surface. The texture evolution phenomena were then discussed. Nakahara and Felder examined electrodeposited Ni films with transmission electron microscopy (TEM).¹⁵ They emphasized the possible formation of metal hydrides as well as the inclusion of hydroxide.

Dahms and Croll proposed the concept of the surface pH in order to confirm their model that nickel hydroxide works as an inhibitor in the case of Fe-Ni alloy electrodeposition.¹⁶ Deligianni and Romanikw then measured the pH in the neighborhood of the cathode and demonstrated that the surface pH value was actually higher than that in the bulk solution.¹⁷

The texture structure evolution on a polycrystalline substrate was examined in Europe after Fischer.¹⁸ A classification diagram with two coordinates of current density divided by metal-ion concentration and inhibition intensity was proposed by Winand.¹⁹ His diagram may provide a guide to control the microstructural and morphological variations of an electrodeposited film. Unfortunately, his chosen coordinate is qualitative. It would be preferable to describe them in a quantitative manner when the electrochemical processing of tai-

lored materials is carried out, at least on the current density coordinate. The overpotential concept may replace the qualitative coordinate of current density for noble metals, whereas the simultaneous hydrogen gas evolution must be taken into account for the electrodeposition of iron group transition metals. Thus, the pH value at the cathode surface may provide an additional coordinate.

It is the present objective to understand the electrodeposition reaction mechanism of Ni^{2+} ions onto a vertical plane substrate immersed in a stagnant electrolyte. One of the key issues is to correlate the surface pH value to the orientation index of the electrodeposited film.

Experimental

Ni was electrodeposited from a Watts bath containing 262 g L^{-1} $\text{NiSO}_4 \cdot 6\text{H}_2\text{O}$, 45 g L^{-1} $\text{NiCl}_2 \cdot 6\text{H}_2\text{O}$, and 38 g L^{-1} H_3BO_3 (pH 3.4) at room temperature. The pH value was adjusted by adding H_2SO_4 or NaOH aqueous solutions. The vertical cathode was fabricated from a rolled silver sheet and the anode from a nickel sheet. The effective surface area of both electrodes was 1×1 cm. The vertical plane anode surface was installed parallel to the cathode. Prior to each experiment, the substrate was ultrasonically cleaned sequentially in acetone, ethanol, and distilled water for 15 min. The grain size of Ag substrate was less than 1 μm . Electrodeposition was conducted potentiostatically at potentials from $E = -0.8$ to -1.6 V with respect to a Ag/AgCl , KCl sat. [$E = +0.20$ V vs standard hydrogen electrode (SHE)] reference electrode. The bulk pH values were varied from 1.5 to 5.5.

Working and counter electrodes were configured face to face on the inner walls of the electrolysis cell. The reference electrode was placed close to the silver working electrode using a Luggin capillary. The amount of charge passed was maintained at 150 C cm^{-2} . It would correspond to 35–50 μm film thickness under the presumptions of uniformly and densely precipitated films without any void fraction and current efficiency over 70%. After experiments, the electrodeposited Ni specimens were cleaned carefully with distilled water, dried, and weighed. The partial current density for Ni electrodeposition was calculated from the mass of Ni electrodeposits, which was determined gravimetrically and was directly converted to current efficiency. The crystal orientation of the electrodeposited film was examined by X-ray powder diffraction using $\text{Co K}\alpha$ radiation.

Results and Discussion

Polarization curve and current efficiency.—Figure 1 shows the polarization curve measured in the solutions at pH 1.5, 3.4, and 5.5. The current density increased almost linearly from 10 to 160 mA cm^{-2} at pH 1.5. In the higher pH (3.4, 5.5) solutions, the current density increases with decreasing potential almost in a par-

* Electrochemical Society Active Member.

^z E-mail: fukunaka@energy.kyoto-u.ac.jp

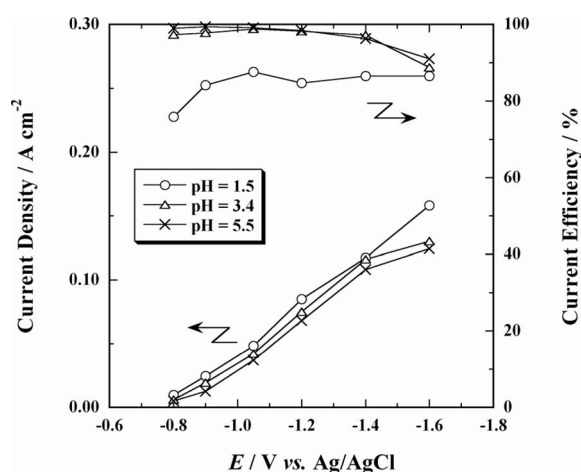


Figure 1. Polarization curves and current efficiencies during electrodeposition in a Watts bath.

allel way among electrolytes with three pH values in the potential range from -0.8 to -1.4 V. The current density is larger at the lower pH. However, the tendency of the current density to increase is significantly suppressed at $E = -1.6$ V.

Because the equilibrium potential of the electrochemical reaction $\text{Ni}^{2+} + 2e^- = \text{Ni}$ is $E^\circ = -0.23$ V vs SHE, H_2 gas evolution always accompanies Ni electrodeposition from a thermodynamic perspective. The current efficiency is less than 100% within the range examined in this work (see Fig. 1). Ni metal electrodeposition is conventionally carried out in a solution at such high pH as to restrict H_2 gas evolution, but doing so induces more nickel hydroxide formation under a higher pH condition. A Watts bath for the industrial Ni metal electrodeposition is hence adjusted to pH 3–5 and boric acid is always added as a pH buffer.

Figure 1 illustrates that the current efficiency is 76% at $E = -0.8$ V and then increases to 84% at $E = -0.9$ V in the lowest pH (1.5) solution. This means that the partial current density for Ni electrodeposition increases more rapidly than that for H_2 evolution. In the more negative potential range, the current efficiency remains 84–87%. In contrast, a nearly 100% efficiency is maintained at pH 3.4 and 5.5, which are close to the pH value for industrial electroplating. These pH solutions show almost the same results as 97–99% efficiency over $E = -0.8$ to -1.2 V, but the efficiency decreases to 90% at $E = -1.6$ V.

The limiting current density on a vertical plane cathode immersed in a semi-infinite stagnant electrolyte is calculated by Eq. 1 from the similarity profile principle.^{20–22}

$$\text{Sh}_y = 0.499\text{Ra}_y^{1/4} \quad [1]$$

where Sh_y and Ra_y are Sherwood number and Rayleigh number, respectively. No H_2 gas evolution is presumed. The limiting current density (i_L) of about 0.30 A cm^{-2} is given by $\Theta = c(=1.19 \text{ mol L}^{-1})$ (see Appendix A). Numerical values of Ni^{2+} ions are listed in Table I. It is a little questionable to accept the

Table I. Numerical values for Ni^{2+} ions used in the calculation.^a

| | | Reference |
|---------------------------------------------|-----------------------|-----------|
| D ($\text{cm}^2 \text{ s}^{-1}$) | 6.9×10^{-6} | 16 |
| t (-) | 0.4 | 23 |
| μ ($\text{g cm}^{-1} \text{ s}^{-1}$) | 1.77×10^{-2} | 24 |
| α ($\text{cm}^3 \text{ mol}^{-1}$) | 1.23×10^2 | 25 |

^a Viscosity and densification coefficient are estimated in the electrolyte solution containing only NiSO_4 .

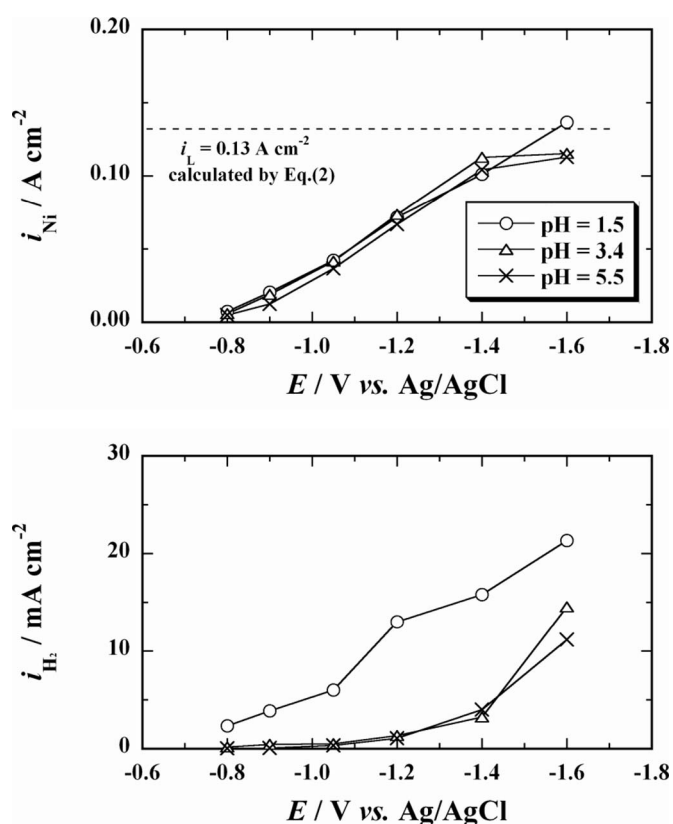


Figure 2. Variations of the partial current densities for Ni electrodeposition, i_{Ni} , and H_2 gas evolution, i_{H_2} , with the electrode potential.

hypothesis of the semi-infinite model in direction to anode, because the natural convection is induced significantly at high current density. The effect of the counter electrode must be taken into account²⁶ because the anode–cathode distance is only 1 cm. With an effective concentration boundary layer thickness (δ) of 100–200 μm , the limiting current density is calculated to be 0.13 – 0.26 A cm^{-2} by the following equation

$$i_L = zFD \frac{c}{(1-i)\delta} \quad [2]$$

This calculated limiting current density still looks high. Suppressing the dependence of i on electrode potential at $E = -1.6$ V may be understood not only in the mass-transfer mechanism, but also in the other chemical transfers that are described later.

Figure 2 shows the partial current densities for Ni electrodeposition (i_{Ni}) and H_2 gas evolution (i_{H_2}). The i_{Ni} at pH 5.5 is slightly lower than the other ones, particularly at potentials more positive than $E = -1.4$ V as the pH dependence of i is similarly demonstrated in Fig. 1. That may be caused by lowered Ni^{2+} concentration due to the complexes formation as $\text{Ni}_4(\text{OH})_4^{4+27,28}$ as well as the difference of the electrolyte conductivity (pH 1.5: 0.059 S cm^{-1} , pH 3.4: 0.051 S cm^{-1} , pH 5.5: 0.050 S cm^{-1}). The current density (i_{Ni}) continues to increase even above 0.10 A cm^{-2} at pH 1.5. The H_2 gas evolution rate has a significant role in enhancing the cathodic mass-transfer coefficient^{29–31} because it promotes the natural convection.

The i_{H_2} at pH 3.4 and 5.5 is always smaller than at pH 1.5. Such a difference is partly caused by the pH dependence of an equilibrium electrode potential of H^+/H_2 system.

Preferred orientation.— Figure 3 shows the X-ray diffraction (XRD) patterns of the electrodeposited Ni thin films. The XRD patterns change abruptly when E decreases from -0.9 to -1.05 V at

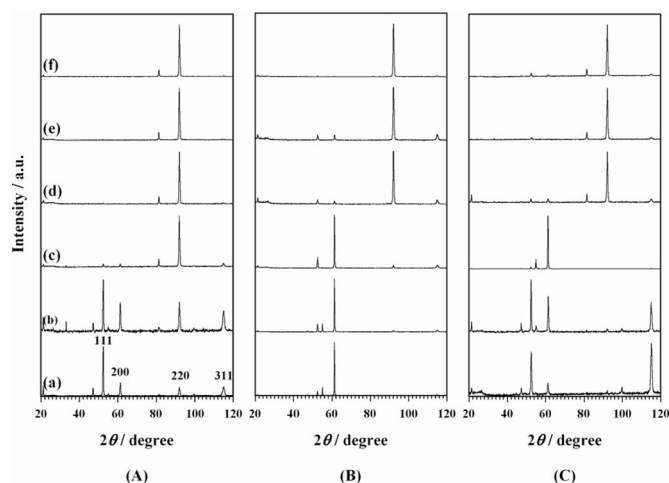


Figure 3. XRD patterns of Ni films electrodeposited at $E =$ (a) -0.8 , (b) -0.9 , (c) -1.05 , (d) -1.2 , (e) -1.4 , and (f) -1.6 V. [The bulk pH values are (A) 1.5, (B) 3.4, and (C) 5.5.]

pH 1.5. The peak intensity ratios observed at $E = -0.8$ V are similar to those in the Joint Committee on Powder Diffraction Standards (JCPDS) powder pattern. The 220 plane peak becomes predominant, and the other peaks almost disappear, in the potential range below -1.05 V.

This kind of microstructural transition in the diffraction pattern also appears when E decreases from -1.05 to -1.2 V at pH 3.4. However, the 200 plane peak becomes predominant before the strong 220 planes peak appears at pH 3.4. The Ni thin film deposited at pH 5.5 is characterized by the relatively strong 311 plane peak at $E = -0.8$ V. Thus, the 220 plane peak generally appears in the high overpotential range in all pH solutions.

The preferred orientation of an electrodeposited film was quantitatively discussed by conveniently defining the orientation index of hkl plane (M_{hkl}).³²

$$M_{hkl} = \frac{I_{hkl} / I_{hkl}^0}{\sum_j I_{h_j k_j l_j} / I_{h_j k_j l_j}^0} \quad [3]$$

where I_{hkl} and I_{hkl}^0 are XRD intensities for the hkl plane of an electrodeposited film and the JCPDS (04-0850) powder pattern, respectively.

Figure 4 shows the preferred orientation index variation of the Ni films as a function of electrode potential. If all crystal planes are oriented in all directions with the same probability as a powder pattern, then the M value is equal to 1. The hkl planes exhibiting M

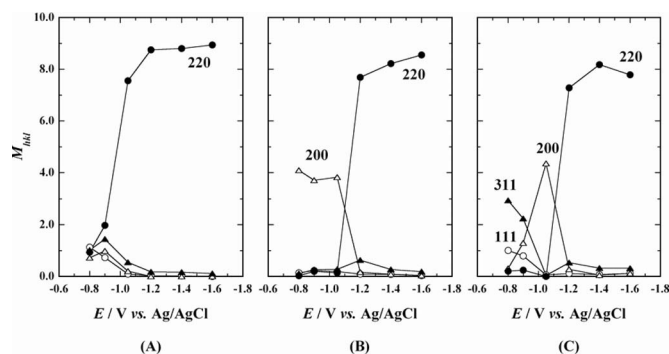
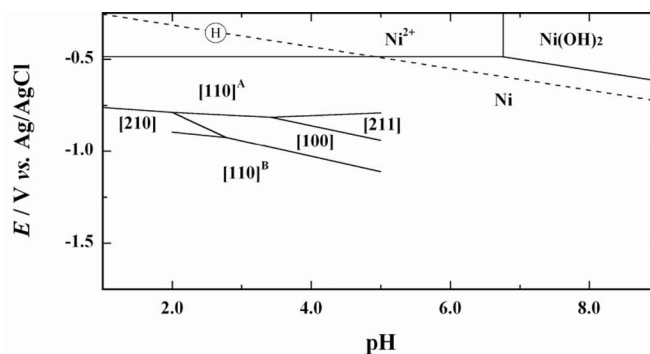
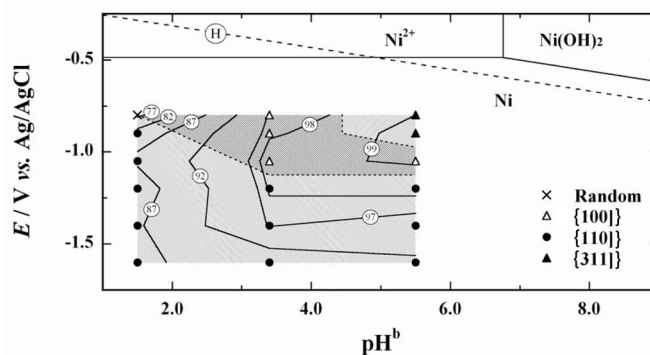


Figure 4. Variations of the orientation indices of Ni films with the electrode potential. [The bulk pH values are (A) 1.5, (B) 3.4, and (C) 5.5.]



(A)



(B)

Figure 5. (A) Texture distribution of electrodeposited Ni thin film in the E -pH diagram³³ reported in Ref. 6. The activity coefficient of Ni^{2+} is approximated as 0.04.³⁴ The broken line indicated by (H) shows the equilibrium potential of H^+/H_2 . (B) Distributions of the current efficiency and the preferred orientation in the E -pH^b diagram. Each inset number from 77 to 99 is assigned to the current efficiency (%). The dotted lines indicate the boundaries between the different preferred orientation domains with shadow areas.

values greater than 1 and less than 1 represent the preferential orientation and the suppressed orientation compared with the powder pattern, respectively.

When the solution pH is 1.5, all crystal planes show M of nearly 1 at $E = -0.8$ V. M_{220} increases abruptly to 8 at $E = -1.05$ V and is thereafter saturated. As a result, the preferential growth of the other planes are completely suppressed more negative than $E = -1.2$ V.

At pH 3.4, only the $\{100\}$ plane is preferentially oriented at $E = -0.8$ to -1.05 V. It is replaced by the $\{110\}$ plane in the potential range below -1.2 V. The orientation indices of the other planes always remain near zero.

The $\{311\}$ preferred orientation with $M_{311} = 2-3$ is seen at $E = -0.8$ and -0.9 V at pH 5.5. The other planes are not completely suppressed. The $\{100\}$ preferred orientation appears only at $E = -1.05$ V.

Appearance of the $\{110\}$ preferred orientation is inevitable as the electrode potential decreases, regardless of pH. It is often pointed out that the adsorbents, e.g., hydrogen adatoms and nickel hydroxide, strongly affect the preferred orientation of electrodeposited Ni films.

The preferred orientation variations were plotted with the current efficiency contour map onto the E -pH diagram in Fig. 5B. They had already been reported by Froment et al.⁶⁻¹⁰ in a similar electrolyte composition ($300 \text{ g L}^{-1} \text{ NiSO}_4 \cdot 7\text{H}_2\text{O}$, $35 \text{ g L}^{-1} \text{ NiCl}_2 \cdot 6\text{H}_2\text{O}$, and $40 \text{ g L}^{-1} \text{ H}_3\text{BO}_3$) (see Fig. 5A). The $[110]$ orientation appears twice with increased cathodic overpotential ($[110]^A$ and $[110]^B$ denote the $[110]$ axis orientations at lower and higher cathodic overpotentials, respectively). The $[210]$ and $[211]$ orientations are separated by the

[100] one in the low- and high-pH regions. They described that the [110]^A, [211], [210], and [110]^B orientations are attributed to the inhibitions by H_{ads}, Ni(OH)₂, H₂ molecules, and both Ni(OH)₂ and H₂ molecules, respectively, and that the [100] texture was evolved by the crystal growth free from any adsorbed species.⁸⁻¹¹

Figure 5B was constructed with the following results. The {311} preferred orientation is located nearest to the region where Ni(OH)₂ is stable.³³ The electrodeposited sample with a {311} preferred orientation showed a gray-colored and smooth surface. The current efficiency is close to 100% at (*E*, pH^b) = (−0.80 V, 5.5) where the {311} orientation exists. The {100} orientation area surrounds the {311} area. A random orientation is prevalent in the lowest pH and the most positive potential corner.

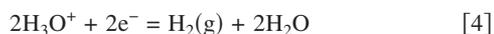
In the present work, the [110]^A orientation was not confirmed because the electrodeposition was not conducted at more positive potentials than *E* = −0.8 V. The {311} orientation is found in the domain where the [211] orientation prevails in Fig. 5A. The random orientation at (*E*, pH) = (−0.80 V, 1.5) appears in the domains of the [210] orientation in Fig. 5A. The [110] orientation becomes predominant with increased the cathodic overpotential in Fig. 5A and B. The definition of the crystal preferred orientation plane is slightly different between the reports by Froment et al. and this paper. It must be emphasized, however, that the transition boundary lines between the [100] and [110]^B orientations similarly locate in both *E*-pH diagrams.

Along the pH axis from (−0.80 V, 5.5) to (−0.80 V, 1.5), the current efficiency decreases from 99 to 76%. The {311} orientation changes through the {100} orientation and finally reaches a random orientation at the lowest current efficiency of 77%.

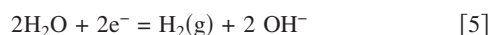
Additionally, this {311} orientation changes to the {110} orientation through the {100} orientation domain along the *E* axis from (−0.80 V, 5.5) through (−1.6 V, 5.5) and then toward the (−1.6 V, 1.5) corner. The current efficiency gradually decreases from 91 to 87% along this trajectory line.

Figure 5B indicates that the transition of the preferred orientation plane may not perfectly accommodate the current efficiency contour map in the two-dimensional *E*-pH map.

Surface pH.—Dahms and Croll tried to understand the anomalous codeposition of Fe–Ni alloys by introducing the possibility of nickel hydroxide formation as an inhibitor.¹⁶ They evaluated the pH value at the cathode surface based on the diffusion model combined with hydrolysis reactions of metal ions. The pH at the cathode surface remains an interesting subject for the researchers to examine the electrodeposition mechanism of transition metals.^{28,35-37} The pH value at the cathode surface changes due to the overall reactions



and

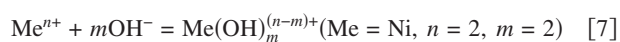


Both processes may take place at nickel electrodes.

The diffusion process tends to compensate the pH variations at the interface. The H₃O⁺ and buffer species must be considered. Any species reacting with H₃O⁺ or OH[−] exhibits a buffering function through the reactions as



In addition, hydrolysis reactions



must be considered.

The diffusion of all buffering species can be treated in the same way by taking into account the one-dimensional diffusion normal to the cathode surface. In the subsequent treatment, the species H_{*n*}A therefore represents hydrolysis products as well.

For a steady-state one-dimensional diffusion process inside a particular concentration boundary layer thickness normal to a plane electrode, we can express the flux as

$$\frac{i_{\text{H}_2}}{F} = D_{\text{H}^+} \frac{\partial C_{\text{H}^+}}{\partial x} \Big|_{x=0} - D_{\text{OH}^-} \frac{\partial C_{\text{OH}^-}}{\partial x} \Big|_{x=0} + nD_{\text{H}_n\text{A}} \frac{\partial C_{\text{H}_n\text{A}}}{\partial x} \Big|_{x=0} \quad [8]$$

where *i*_{H₂} is the current density for H₂ gas evolution due to Reactions 4 and 5; *F* is Faraday constant; *D*_{H⁺}, *D*_{OH[−]}, and *D*_{H_{*n*}A} are diffusion coefficients of H⁺ ions, OH[−] ions, and buffering species H_{*n*}A, respectively; *C*_{*i*} is the concentration of species (*i*); and *x* is the distance normal to the electrode plane.

We can substitute *C*_{OH[−]} and *C*_{H_{*n*}A} in Eq. 8 by using the relations

$$C_{\text{H}^+}C_{\text{OH}^-} = K_{\text{W}} \quad [9]$$

$$C_{\text{H}^+}^n C_{\text{A}^{n-}} = K_{\text{H}} \times C_{\text{H}_n\text{A}} \quad [10]$$

and

$$C = C_{\text{H}_n\text{A}} + C_{\text{A}^{n-}} \quad [11]$$

where *K*_W is the autoprotolysis constant of water; *K*_H, the dissociation constant of buffer; *C*, total concentration of buffer components; *C*_{H_{*n*}A}, the concentration of undissociated buffer acid; *C*_{A^{*n*−}}, the concentration of buffer anion. Eq. 8 is now rearranged as

$$\frac{i_{\text{H}_2}}{F} = D_{\text{H}^+} \frac{\partial C_{\text{H}^+}}{\partial x} + \frac{D_{\text{OH}^-}K_{\text{W}}}{C_{\text{H}^+}^2} \frac{\partial C_{\text{H}^+}}{\partial x} + n^2D_{\text{H}_n\text{A}} \frac{CC_{\text{H}^+}^{n-1}K_{\text{H}}}{(K_{\text{H}} + C_{\text{H}^+})^2} \frac{\partial C_{\text{H}^+}}{\partial x} \quad [12]$$

Equation 12 must be integrated over the distance between the electrode surface (*x* = 0, *C*_{H⁺} = *C*_{H⁺}^s) and the outer edge of the “diffusion layer” (*x* = δ_{H⁺}, *C*_{H⁺} = *C*_{H⁺}^b). Appendix B describes how to determine the diffusion layer thickness.

As the first-order approximation, we introduce an identical diffusion layer thickness for all species in order to integrate Eq. 12. This approximation gives Eq. 13

$$\frac{i_{\text{H}_2}}{F}\delta_{\text{H}^+} = D_{\text{H}^+}(C_{\text{H}^+}^{\text{b}} - C_{\text{H}^+}^{\text{s}}) + D_{\text{OH}^-}K_{\text{W}} \frac{C_{\text{H}^+}^{\text{b}} - C_{\text{H}^+}^{\text{s}}}{C_{\text{H}^+}^{\text{b}}C_{\text{H}^+}^{\text{s}}} + nD_{\text{H}_n\text{A}}K_{\text{H}}C \frac{(C_{\text{H}^+}^{\text{b}})^n - (C_{\text{H}^+}^{\text{s}})^n}{\{K_{\text{H}} + (C_{\text{H}^+}^{\text{b}})^n\}\{K_{\text{H}} + (C_{\text{H}^+}^{\text{s}})^n\}} \quad [13]$$

where it is assumed for the simplicity of calculation that the variation of buffer species concentration *C* with *x* is negligibly small. This assumption is acceptable because the diffusion layer thickness is only 100–200 μm and the partial current density is relatively small.

In this system, the candidate species for the buffer acids are HSO₄[−], H₃BO₃, and Ni₄(OH)₄⁴⁺. It was reported that Ni₄(OH)₄⁴⁺ is predominant rather than NiOH⁺ among the Ni²⁺ complexes in the concentrated solution.^{27,28} The first species stems from H₂SO₄ as the pH adjuster only when the pH is set to 1.5. Thus, *n*, H_{*n*}A, and A^{*n*−} represent one, HSO₄[−], and SO₄^{2−}, respectively. The amount of neutral species H₂SO₄ is assumed to be zero due to the complete dissociation of the first step reaction (see Appendix C).

The third term on the right side in Eq. 13 cannot be applied to H₃BO₃ and Ni₄(OH)₄⁴⁺ because those dissociation reactions do not follow the type of Eq. 6.

The dissociation mechanism of H₃BO₃ is rather complicated. The role of boric acid to catalyze the Ni electrodeposition reaction in a nickel sulfate solution was often pointed out.³⁸⁻⁴¹ In the present paper, only the buffering action of boric acid is considered. The literature³³ describes the following ten equilibrium reactions in the aqueous system



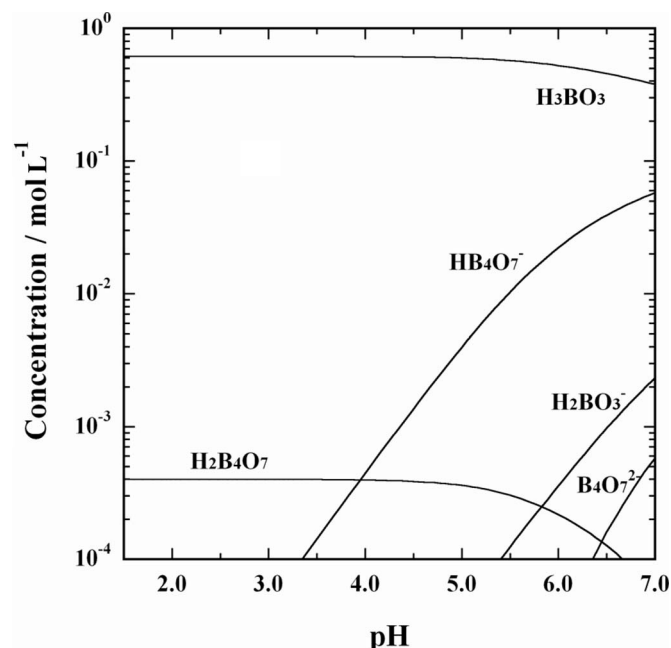
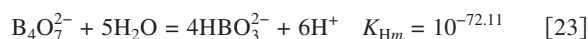
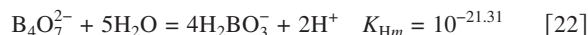


Figure 6. Concentration distribution of the soluble species from boric acid.



K_{Hm} ($m = 1, \dots, 10$) is the stability constant where the unit of concentration is molarity. Figure 6 shows the concentration distribution of soluble species from H_3BO_3 depending on the pH neglecting the activity coefficients.

The total concentration of H_3BO_3 added in the electrolyte solution is 0.62 mol L^{-1} . It is clearly observed that H_3BO_3 barely dissociates up to about pH 5. Above this pH value, the concentration of H_3BO_3 starts to decrease significantly and HB_4O_7^- from Eq. 19 gradually increases.

H_2BO_3^- is generated by Eq. 14 above pH 5.5. $\text{B}_4\text{O}_7^{2-}$ stemming from Eq. 20 and 21 appears above pH 6.3. A constant concentration of $\text{H}_2\text{B}_4\text{O}_7$ is maintained up to pH 5. It decreases corresponding to the behavior of H_3BO_3 due to Eq. 17, though it does not have a buffering function.

Consequently, the buffer effect of H_3BO_3 must be considered based on the simultaneous dissociating reactions. Thus, it needs to be rewritten as the appropriate form for H_3BO_3 including the several buffer reactions. The primary reactions to be considered are Eq. 14, 19, and 21.

Therefore, n can be written by

$$n = -\frac{\partial C_{\text{H}_2\text{BO}_3^-}}{\partial C_{\text{H}_3\text{BO}_3}} - \frac{\partial C_{\text{HB}_4\text{O}_7^-}}{\partial C_{\text{H}_3\text{BO}_3}} - 2\frac{\partial C_{\text{B}_4\text{O}_7^{2-}}}{\partial C_{\text{H}_3\text{BO}_3}} \quad [24]$$

As a result

Table II. Diffusion coefficients used in the calculation.

| Species | Diffusion coefficient ($\text{cm}^2 \text{ s}^{-1}$) | Reference |
|---------------------------------|--------------------------------------------------------|-----------|
| H^+ | 5.0×10^{-5} | 42 |
| OH^- | 1.0×10^{-5} | 42 |
| HSO_4^- | 1.1×10^{-5} | 16 |
| H_3BO_3 | 1.1×10^{-5} | 43 |
| $\text{Ni}_4(\text{OH})_4^{4+}$ | 4.3×10^{-6} | 28 |

$$nD_{\text{H}_3\text{BO}_3} \frac{\partial C_{\text{H}_3\text{BO}_3}}{\partial x} = -D_{\text{H}_3\text{BO}_3} \left(\frac{\partial C_{\text{H}_2\text{BO}_3^-}}{\partial x} + \frac{\partial C_{\text{HB}_4\text{O}_7^-}}{\partial x} + 2\frac{\partial C_{\text{B}_4\text{O}_7^{2-}}}{\partial x} \right) \quad [25]$$

where the total concentration of H_3BO_3 ($C = 0.62 \text{ mol L}^{-1}$) is assumed constant at the cathode surface ($x = 0$) and in the bulk phase ($x \geq \delta_{\text{H}^+}$) as described previously.

The molarity-based stability constants of $\text{Ni}_4(\text{OH})_4^{4+}$ (K_{N1}) and NiOH^+ (K_{N2}) are listed below²⁸



The concentration of NiOH^+ is always small enough to be neglected within the range of pH examined in this paper, which coincides with Murthy et al.²⁸

The diffusion flux of $4D_{\text{Ni}_4(\text{OH})_4^{4+}}(\partial C_{\text{Ni}_4(\text{OH})_4^{4+}}/\partial x)_{x=0}$ potentially contained in Eq. 8 includes $C_{\text{Ni}^{2+}}$ through i_{Ni} as follows

$$\frac{i_{\text{Ni}}(1-t)}{2F} = D_{\text{Ni}^{2+}} \frac{\partial C_{\text{Ni}^{2+}}}{\partial x} \Big|_{x=0} + 4D_{\text{Ni}_4(\text{OH})_4^{4+}} \frac{\partial C_{\text{Ni}_4(\text{OH})_4^{4+}}}{\partial x} \Big|_{x=0} \quad [28]$$

and

$$C_{\text{Ni}_4(\text{OH})_4^{4+}} = \left(\frac{C_{\text{Ni}^{2+}} K_{\text{W}}}{C_{\text{H}^+} K_{\text{N1}}} \right)^4 \quad [29]$$

The ionic flux due to the migration mechanism is approximated by $i_{\text{Ni}}t/zF$.²⁰⁻²² Then the concentrations of H^+ and Ni^{2+} at $x = 0$ ($C_{\text{H}^+}^s$, $C_{\text{Ni}^{2+}}^s$) are given by the optimal solutions of Eq. 8 and 28, and the mass balance equation of H_3BO_3 . The diffusion coefficient of each chemical species is listed in Table II. The diffusivity of $\text{Ni}_4(\text{OH})_4^{4+}$ was taken from the literature.²⁸

Figure 7 shows the variations of the surface pH (pH^s). When the bulk pH (pH^b) is 1.5, the pH^s gradually increases with the H_2 gas evolution rate and then abruptly jumps to 6 above $i_{\text{H}_2} = 12 \text{ mA cm}^{-2}$ like a typical pH titration curve.

At pH^b 3.4, the pH^s increases immediately after i_{H_2} is generated, in contrast to the case of pH^b 1.5. The pH^s already reaches 6.0 even at $i_{\text{H}_2} = 1 \text{ mA cm}^{-2}$. H_3BO_3 must dissociate to a significant extent near the cathode surface in such a case, according to Fig. 6. At pH^b 5.5, three stages are noticed in the variation of the preferred orientation in Fig. 5. The pH^s gradually increases and reaches 6.8 at $E = -1.4 \text{ V}$.

Figure 7 demonstrates that the transition to the {110} preferred orientation is completed within the i_{H_2} of few mA cm^{-2} in all pH solutions.

The suppression of the i_{Ni} at $E = -1.6 \text{ V}$ at pH 3.4 and 5.5 in Fig. 2 is probably due to the shift of the ionic equilibrium at the cathode surface to reduce the concentration of Ni^{2+} and generate $\text{Ni}_4(\text{OH})_4^{4+}$ or $\text{Ni}(\text{OH})_2$. The ionic products of $C_{\text{Ni}^{2+}}$ and $C_{\text{OH}^-}^2$ at $x = 0$ are calculated to be about $10^{-16} (\text{mol}^3 \text{ L}^{-3})$, taking the activity coefficients³⁴ into consideration. This is equivalent to the solubility

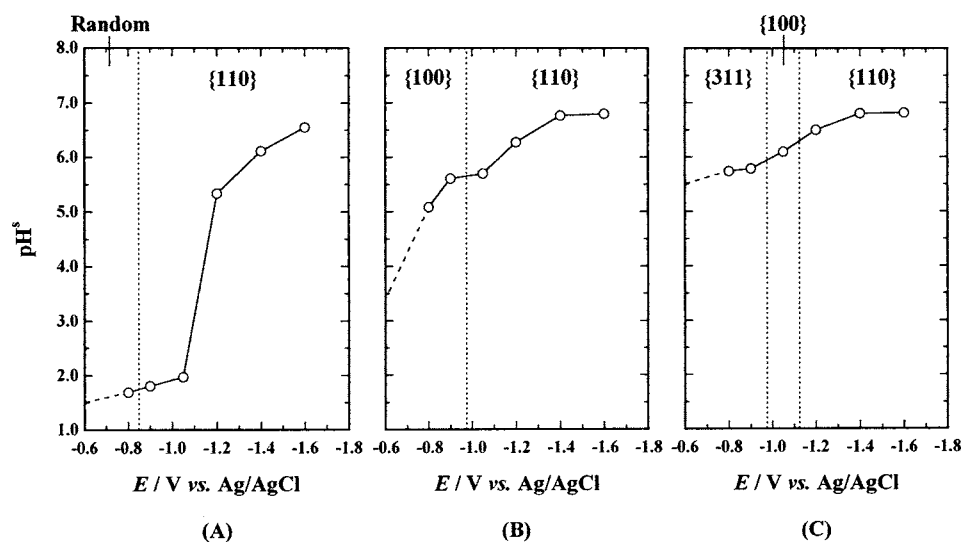


Figure 7. Relation between electrode potential and pH^s calculated electrode potential. [The bulk pH values are (A) 1.5, (B) 3.4, and (C) 5.5.]

product of $\text{Ni}(\text{OH})_2$ of 10^{-16} – 10^{-14} .^{16,28,33,37} Moreover, the conductivity variation due to the electrolyte composition may also participate in the phenomenon appearing in Fig. 2.

Figure 8 rearranges Fig. 5 by introducing the concept of the surface pH value (pH^s). The {311} orientation domain is shrunk toward the higher pH region. It is found that the transition boundary between the preferred orientations {100} and {110} is located about 500 mV below the H^+/H_2 equilibrium potential line ($\eta_{\text{H}_2} = 500$ mV). Moreover, a ridge in the current efficiency contour map is apparently running parallel to this transition boundary line. It is reported that hydrogen overpotential is roughly 200 mV on a Ni metal substrate.^{44,45} A significant rate of i_{H_2} thus introduces a tremendous amount of dissolved H atoms (into Ni metal). This deduction reaction probably results in the transition from {100} to {110}, which may be due to the residual strain around the interstitial H atoms. This appears to support the postulate that the texture evolution phenomena of the transition metals are partly influenced by the H_2 gas evolution as the competitive reaction on the depositing Ni metal cathode surface.

Amblard et al. ascribed the [110]^B texture to both adsorbed species of H_2 molecule and $\text{Ni}(\text{OH})_2$,^{8,11} but their discussion was essentially obscure. Another implicated mechanism caused by nickel adatoms was also proposed.¹³ The soundness of such deductions is further beyond the present characterization technique. The present contribution to this problem is to introduce the surface pH concept in comparison with the past qualitative discussion. The kinetic model on the competitive reaction during Ni electrocrystallization

introduces the surface coverage concept quantitatively combined with the surface concentrations of chemical species in the next step of our research.

Conclusion

Ni metal was electrodeposited on the vertical plane cathode in three different pH solutions. The polarization curve showed a clear pH dependence. The current efficiency varied from 70 to 83% at pH 1.5. H_2 gas evolution might enhance the cathodic mass-transfer rate of Ni^{2+} ions significantly at pH 1.5. However, it was always close to 100% and slightly depressed at potentials more negative than $E = -1.4$ V at pH 3.4 and 5.5.

In the low-overpotential range, the preferred crystal orientation of electrodeposited Ni films varied depending on the pH. The {110} preferred orientation only appeared in the more negative potential range, regardless of pH.

The surface pH at the cathode (pH^s) was then calculated using the measured partial current density for H_2 gas evolution based on a one-dimensional mass-transfer model that included the buffer action. The calculated pH^s jumped abruptly above 6 as i_{H_2} increased.

The transition of the preferred orientation was plotted with a current efficiency contour line in the E - pH^s map. The transition boundary of the preferred orientation from {100} to {110} was located almost parallel with the equilibrium H_2 gas evolution line. This behavior may support the postulate that the dissolved hydrogen atoms in Ni metal are partly responsible for controlling the texture structure evolution.

Acknowledgments

The authors thank Dr. F. McLarnon, Dr. S. Nakahara, and Dr. S. Kikuchi for their valuable discussions throughout the present works. Part of this work was carried out under financial assistance given to Y.F. by the Ministry of Education, Science, Sports, and Culture (project no. 15360402), for which the authors are grateful.

Kyoto University assisted in meeting the publication costs of this article.

Appendix A

The Rayleigh number can be written by

$$\text{Ra}_v = \frac{g\alpha c y^3}{\nu D} \quad [\text{A-1}]$$

where g , α , c , y , ν , and D are gravitational acceleration (cm s^{-2}), densification coefficient ($\text{cm}^3 \text{mol}^{-1}$), bulk concentration (mol L^{-1}), vertical distance from lower edge (cm), kinematic viscosity ($\text{cm}^2 \text{s}^{-1}$), and diffusivity ($\text{cm}^2 \text{s}^{-1}$), respectively. The Sherwood number was

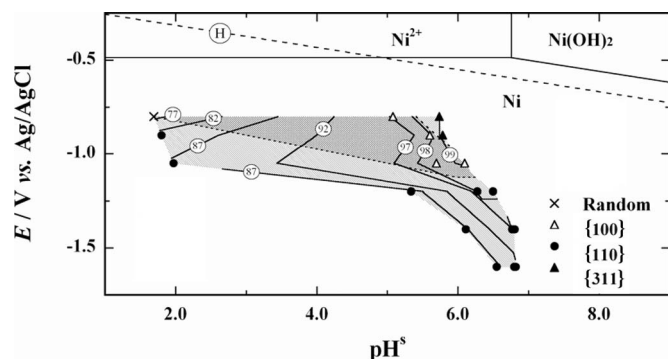


Figure 8. Distributions of the current efficiency and the preferred orientation in the E - pH^s diagram.

$$Sh_y = \frac{i_y(1-t)y}{zFD\Theta} \quad [\text{A-2}]$$

where i_y , t , z , F , and Θ are local current density at y (A cm^{-2}), transference number (-), valency number (-), Faraday constant (C mol^{-1}), and difference of the surface concentration from the bulk concentration (mol L^{-1}), respectively. The Θ at a given i_y can be evaluated by using the correlation equation of Eq. 1.

Appendix B

The cathodic mass-transfer rate is enhanced by H_2 gas bubble evolution. Fukunaka et al. measured the variations of the mass-transfer coefficient, rising velocity of gas bubbles, and thickness of bubble dispersion layer along a vertical direction with current density.³¹ The measured ionic mass-transfer coefficient was analyzed by applying the additivity rule of micro- and macromixing proposed by Alkire and Lu.³⁰ Micromixing is induced by the microconvective flow of electrolyte during bubble growth and detachment on the cathode surface. Macromixing refers to the turbulent natural convection induced by the density difference between the electrolyte at the cathode surface and the bulk electrolyte. The diffusion layer thickness is given by

$$\delta_{\text{Ni}^{2+}} = \frac{D_{\text{Ni}^{2+}}}{k_m} \quad [\text{B-1}]$$

where $k_m = k_b + k_{in}$; k_b and k_{in} are the mass-transfer coefficient due to micromixing and the mass-transfer coefficient under laminar natural convection, respectively. The latter is assumed to be governed by the void fraction during H_2 evolution.

Within the range of i_{H_2} examined in this study, the possibility of introducing turbulent natural convection is discarded because of $\log Ra_a \leq 5.5$. The ratio of the diffusion layer thickness of H^+ to that of Ni^{2+} is approximated to the case of Cu^{2+}

$$\delta_{\text{H}^+} = \sigma \delta_{\text{Ni}^{2+}} \quad [\text{B-2}]$$

where σ denotes the ratio $\delta_{\text{H}^+}/\delta_{\text{Ni}^{2+}} = 1.25$.^{31,46,47} These equations are used to estimate the diffusion layer thickness of the ions.

Appendix C

Adding sulfuric acid of 2×10^{-2} (mol L^{-1}) in a Watts bath reduces the pH by 1.5. Then the H^+ concentration increment is $10^{-1.5} - 10^{-3.4} = 3.1 \times 10^{-2}$ (mol L^{-1}). Assuming that the H^+ concentration increment contributed by



is 2×10^{-2} (mol L^{-1}), the additional amount of 1.1×10^{-2} (mol L^{-1}) must be compensated as follows



Boric acid does not release H^+ ions in this pH region according to Fig. 6. Finally, the presence of HSO_4^- ions of 0.9×10^{-2} (mol L^{-1}) in the bulk is expected.

References

- N. V. Myung, D.-Y. Park, B.-Y. Yoo, and P. T. A. Sumodjo, *J. Magn. Magn. Mater.*, **265**, 189 (2003).
- G. Gubbiotti, G. Carlotti, S. Tacchi, Y.-K. Liu, C. Scheck, R. Schad, and G. Zangari, *J. Appl. Phys.*, **10**, 10J102 (2005).
- X. Liu, P. Evans, and G. Zangari, *IEEE Trans. Magn.*, **36**, 3479 (2000).
- K. P. Larsen, A. A. Rasmussen, J. T. Ravnkilde, M. Ginnerup, and O. Hansen, *Sens. Actuators, A*, **103**, 156 (2003).
- X. Liu and G. Zangari, *IEEE Trans. Magn.*, **37**, 1764 (2001).
- M. Froment and G. Maurin, *J. Microsc.*, **7**, 39 (1968).
- M. Froment and J. Thevenin, *Electrochim. Acta*, **20**, 877 (1975).
- J. Amblard, M. Froment, and N. Spyrellis, *Surf. Technol.*, **5**, 205 (1977).
- J. Amblard, I. Epelboin, M. Froment, and G. Maurin, *J. Appl. Electrochem.*, **9**, 233 (1979).
- J. Amblard, M. Froment, G. Maurin, N. Spyrellis, and E. T.-Souteyrand, *Electrochim. Acta*, **28**, 909 (1983).
- C. Kollia and N. Spyrellis, *Surf. Coat. Technol.*, **57**, 71 (1993).
- E. Gómez, R. Pollina, and E. Vallés, *J. Electroanal. Chem.*, **386**, 45 (1995).
- H. S. Karayannis and G. Paternaraki, *Electrochim. Acta*, **40**, 1079 (1995).
- A. M. El-Sherik, U. Erb, and J. Page, *Surf. Coat. Technol.*, **88**, 70 (1996).
- S. Nakahara and E. C. Felder, *J. Electrochem. Soc.*, **129**, 45 (1982).
- H. Dahms and I. M. Croll, *J. Electrochem. Soc.*, **112**, 771 (1965).
- H. Deligianni and L. T. Romankiw, *IBM J. Res. Dev.*, **37**, 85 (1993).
- H. Fischer, *Angew. Chem., Int. Ed. Engl.*, **8**, 108 (1969).
- R. Winand, *Trans. Inst. Min. Metall., Sect. C*, **84**, 67 (1975).
- C. Wagner, *J. Electrochem. Soc.*, **95**, 161 (1949).
- C. R. Wilke, M. Eisenberg, and C. W. Tobias, *J. Electrochem. Soc.*, **100**, 513 (1953).
- Y. Fukunaka, T. Minegishi, N. Nishioka, and Y. Kondo, *J. Electrochem. Soc.*, **128**, 1274 (1981).
- A. H. DuRose, *Plat. Surf. Finish.*, 48 (1977).
- S. Alamelu and C. V. Suryanarayana, *Acta Chim. Acad. Sci. Hung.*, **20**, 7 (1959).
- R. Wu, M. Olliazadeh and A. M. Alfantazi, *J. Appl. Electrochem.*, **33**, 1043 (2003).
- K. Denpo, S. Teruta, Y. Fukunaka, and Y. Kondo, *Metall. Trans. B*, **14B**, 633 (1983).
- C. C. Streinz, A. P. Hartman, S. Motupally, and J. W. Weidner, *J. Electrochem. Soc.*, **142**, 1084 (1995).
- M. Murthy, G. S. Nagarajan, J. W. Weidner, and J. W. Van Zee, *J. Electrochem. Soc.*, **143**, 2319 (1996).
- V. A. Ettel, B. V. Tilak, and A. S. Gendron, *J. Electrochem. Soc.*, **121**, 867 (1974).
- R. Alkire and P.-Y. Lu, *J. Electrochem. Soc.*, **126**, 2118 (1979).
- Y. Fukunaka, K. Suzuki, A. Ueda, and Y. Kondo, *J. Electrochem. Soc.*, **136**, 1002 (1989).
- K. S. Willson and J. A. Rogers, *Tech. Proc. Am. Electroplaters Soc.*, **51**, 92 (1964).
- M. Pourbaix, *Atlas of Electrochemical Equilibria in Aqueous Solutions*, Pergamon Press, London (1966).
- M. El Guendouzi, A. Mounir, and A. Dinane, *J. Chem. Thermodyn.*, **35**, 209 (2003).
- M. Matlosz, *J. Electrochem. Soc.*, **140**, 2272 (1993).
- Y. Fukunaka, S. Aikawa, and Z. Asaki, *J. Electrochem. Soc.*, **141**, 1783 (1994).
- N. Zech and D. Landolt, *Electrochim. Acta*, **45**, 3461 (2000).
- J. Horkans, *J. Electrochem. Soc.*, **126**, 1861 (1979).
- J. P. Hoare, *J. Electrochem. Soc.*, **133**, 2491 (1986).
- J. P. Hoare, *J. Electrochem. Soc.*, **134**, 3102 (1987).
- M. Y. Abyaneh and M. Hashemi-Pour, *Trans. Inst. Met. Finish.*, **72**, 23 (1993).
- S. Hessami and C. W. Tobias, *J. Electrochem. Soc.*, **136**, 3611 (1989).
- J. K. Park and K. J. Lee, *J. Chem. Eng. Data*, **39**, 891 (1994).
- H. Ezaki, M. Morinaga, and S. Watanabe, *Electrochim. Acta*, **38**, 557 (1993).
- J. Tamm, L. Tamm, and P. Vares, *Russ. J. Electrochem.*, **36**, 1174 (2000).
- Y. Fukunaka, K. Denpo, M. Iwata, K. Maruoka, and Y. Kondo, *J. Electrochem. Soc.*, **130**, 2492 (1983).
- K. Denpo, T. Okumura, Y. Fukunaka, and Y. Kondo, *J. Electrochem. Soc.*, **132**, 1145 (1985).